

Defect-Induced, Ferroelectric-Like Switching and Adjustable Dielectric Tunability in Antiferroelectrics

Hao Pan, Zishen Tian, Megha Acharya, Xiaoxi Huang, Pravin Kavle, Hongrui Zhang, Liyan Wu, Dongfang Chen, John Carroll, Robert Scales, Cedric J. G. Meyers, Kathleen Coleman, Brendan Hanrahan, Jonathan E. Spanier, and Lane W. Martin*

Antiferroelectrics, which undergo a field-induced phase transition to ferroelectric order that manifests as double-hysteresis polarization switching, exhibit great potential for dielectric, electromechanical, and electrothermal applications. Compared to their ferroelectric cousins, however, considerably fewer efforts have been made to understand and control antiferroelectrics. Here, it is demonstrated that the polarization switching behavior of an antiferroelectric can be strongly influenced and effectively regulated by point defects. In films of the canonical antiferroelectric PbZrO_3 , decreasing oxygen pressure during deposition (and thus increasing adatom kinetic energy) causes unexpected “ferroelectric-like” polarization switching although the films remain in the expected antiferroelectric orthorhombic phase. This “ferroelectric-like” switching is correlated with the creation of bombardment-induced point-defect complexes which pin the antiferroelectric–ferroelectric phase boundaries, and thus effectively delay the phase transition under changing field. The effective pinning energy is extracted via temperature-dependent switching-kinetics studies. In turn, by controlling the concentration of defect complexes, the dielectric tunability of the PbZrO_3 can be adjusted, including being able to convert between “positive” and “negative” tunability near zero field. This work reveals the important role and strong capability of defects to engineer antiferroelectrics for new performance and functionalities.

1. Introduction

Antiferroelectrics, such as the prototypical material PbZrO_3 ,^[1,2] possess antipolar order (i.e., antiparallel alignment of lead-cation displacement in PbZrO_3) that can be switched to polar (parallel) order by an external electric field thus producing a reversible antiferroelectric-to-ferroelectric phase transition and a characteristic double polarization–electric-field hysteresis loop.^[3–5] Such a unique field-induced antipolar-to-polar transition endows antiferroelectrics with properties that are of great interest for a range of applications including nonlinear dielectrics,^[6] capacitive-energy storage,^[7,8] electrothermal-energy conversion,^[9] and electromechanical actuation.^[10,11] But to better understand the nature of such phase transitions in antiferroelectrics and to finely engineer the polarization properties for targeted applications requires that one can fabricate high-quality versions of antiferroelectric materials.

For all crystalline materials, compositional and structural defects (e.g., vacancies,

interstitials, anti-sites, defect complexes, extended defects, etc.) are unavoidable (to some extent) and can strongly influence material properties.^[12] This is especially true for complex oxides like the perovskites (which encompass many common (anti-) ferroelectric materials such as PbZrO_3), where large concentrations of various defects can be accommodated,^[13] and remarkable changes of electric, thermal, dielectric, and other properties can be induced.^[14,15] For example, in perovskite ferroelectrics, defects have traditionally been thought to act as shallow traps of charge carriers thus contributing to high leakage currents^[16] and to interact with ferroelectric domain walls thus being deleterious to polarization related properties (e.g., fatigue, aging, and imprint).^[17,18] In turn, extensive efforts have been made to understand, control, and counteract the impact of defects in ferroelectric materials.^[19] Work on “defect engineering” has shown that gaining such control can produce both improved performance and exotic phenomena.^[20,21] For example, strontium deficiency and titanium anti-site defects in paraelectric SrTiO_3 thin films were reported to generate local dipoles and room-temperature ferroelectricity,^[22] dislocations introduced by mechanical creep in ferroelectric BaTiO_3 can provide a strong


H. Pan, Z. Tian, M. Acharya, X. Huang, P. Kavle, H. Zhang, L. W. Martin
Department of Materials Science and Engineering
University of California
Berkeley, CA 94720, USA
E-mail: lwmartin@berkeley.edu

M. Acharya, P. Kavle, L. W. Martin
Materials Sciences Division
Lawrence Berkeley National Laboratory
Berkeley, CA 94720, USA

L. Wu, D. Chen, C. J. G. Meyers, J. E. Spanier
Department of Mechanical Engineering and Mechanics
Drexel University
Philadelphia, PA 19104, USA

J. Carroll, K. Coleman, B. Hanrahan
DEVCOM US Army Research Laboratory
Adelphi, MD 20783, USA

J. Carroll, R. Scales, J. E. Spanier
Department of Electrical and Computer Engineering
Drexel University
Philadelphia, PA 19104, USA

 The ORCID identification number(s) for the author(s) of this article can be found under <https://doi.org/10.1002/adma.202300257>

DOI: 10.1002/adma.202300257

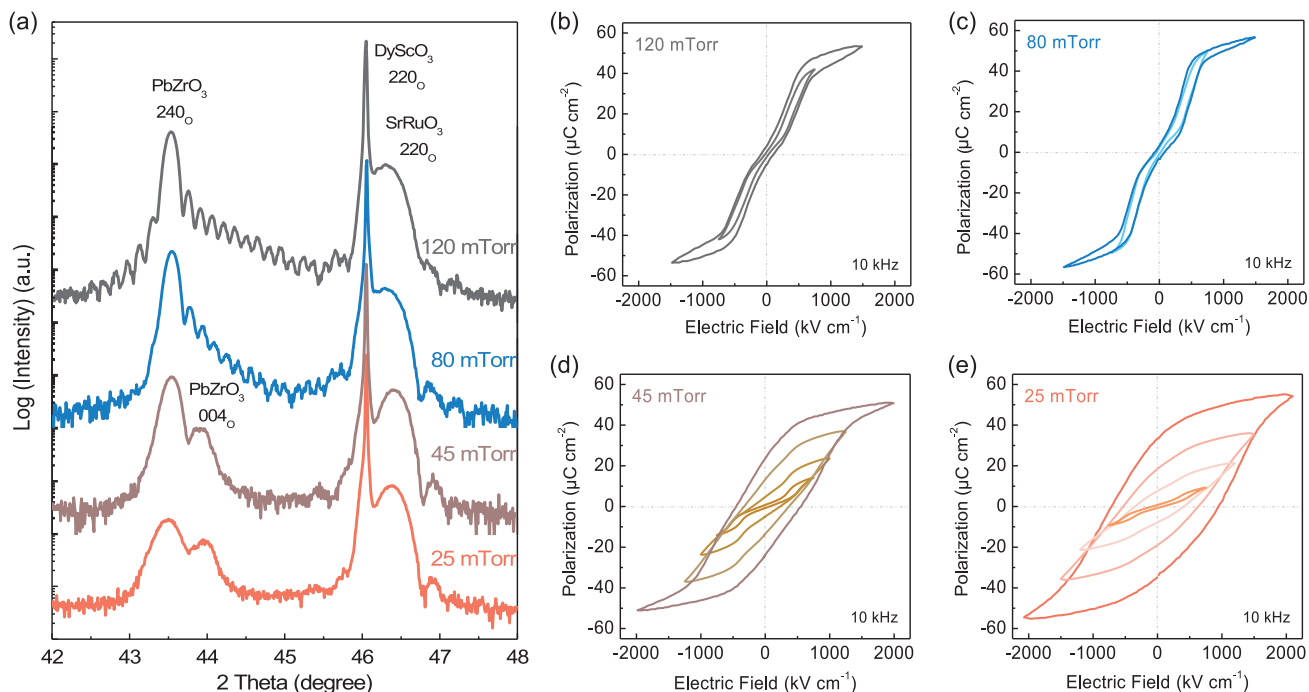


Figure 1. a) X-ray diffraction 2θ - ω scans for the PbZrO₃ heterostructures grown at varying oxygen pressures from (top to bottom) 120, 80, 45, to 25 mTorr. b-e) Polarization-electric field hysteresis loops of PbZrO₃ heterostructures grown at oxygen pressures of 120 mTorr (b), 80 mTorr (c), 45 mTorr (d), and 25 mTorr (e), respectively, measured here at a frequency of 10 kHz.

restoring force for domain-wall displacement thus producing large dielectric and electromechanical responses,^[23] and the introduction of increased intrinsic defect concentrations via ion bombardment can produce deep-level trap states in the relaxor ferroelectric (0.68)PbMg_{1/3}Nb_{2/3}O₃-(0.32)PbTiO₃, which greatly improves resistivity and capacitive-energy storage.^[24] Despite these efforts, considerably less attention has been given to such aspects for antiferroelectrics. It is thus desirable to understand the impact of defects on antiferroelectric properties and to explore defect-based strategies to tailor antiferroelectrics for improved performance and new functionalities.

Here, by varying the oxygen pressure during the pulsed-laser deposition growth process (and thus varying the adatom kinetic energy and subsequent bombardment effects^[20]) defects are deliberately introduced into antiferroelectric PbZrO₃ films. As the growth pressure is gradually decreased from 120 to 25 mTorr, an intriguing evolution of the polarization switching from typical antiferroelectric to “ferroelectric-like” is observed, despite the films remaining in the antiferroelectric (orthorhombic) phase. The “ferroelectric-like” switching is attributed to an increase in the adatom kinetic energy at low growth pressures and the subsequent formation of bombardment-induced point defect complexes, which work to pin the antiferroelectric-to-ferroelectric phase transition boundaries and impact the same transition in both directions. The effective pinning energy is extracted via temperature-dependent polarization switching kinetics studies and found to be 0.11–0.20 eV. Furthermore, it is demonstrated how these defect complexes function as a knob to tailor the dielectric performance of the antiferroelectric. In specific defect-engineered PbZrO₃ films, it is possible to reversibly adjust the dielectric tunability with field poling, thereby effectively convert-

ing between “positive” and “negative” tunability near zero field. This sort of function is uncommon and points the potential for defect-enabled function to open the door to new possibilities.

2. Results and Discussion

A series of 45 nm SrRuO₃/60 nm PbZrO₃/30 nm SrRuO₃/DyScO₃ (110)_o thin-film heterostructures were synthesized via pulsed-laser deposition with various oxygen growth pressures (25, 45, 80, and 120 mTorr) for the PbZrO₃ layer (Experimental Section). Following growth, circular SrRuO₃ top electrodes were fabricated to realize symmetric capacitor structures for electric measurements (Experimental Section). The crystalline structure of the heterostructures was characterized using X-ray diffraction (Experimental Section). Bulk PbZrO₃ possesses an orthorhombic unit cell (lattice parameters $a_o \approx \sqrt{2}a_{pc} \approx 5.872 \text{ \AA}$, $b_o \approx 2\sqrt{2}a_{pc} \approx 11.744 \text{ \AA}$, and $c_o \approx 2c_{pc} \approx 8.202 \text{ \AA}$ where “O” and “pc” denote orthorhombic and pseudocubic cells, respectively).^[25] The PbZrO₃ heterostructures grown under high oxygen growth pressures (i.e., 120 and 80 mTorr) were found to be (240)_o-oriented (i.e., (100)_{pc}- or (010)_{pc}-oriented) from X-ray line scans (top two datasets, Figure 1a), because an in-plane c_o axis is more favored for a smaller lattice mismatch with the DyScO₃ substrate ($a_{pc} \approx b_{pc} \approx 3.945 \text{ \AA}$). In turn, these heterostructures exhibit classic antiferroelectric polarization switching, with double hysteresis loops and antiferroelectric-to-ferroelectric transition fields of $\approx 500 \text{ kV cm}^{-1}$ (Figure 1b,c); similar to previous reports in PbZrO₃ films.^[26,27] Upon decreasing the oxygen growth pressure to 45 and 25 mTorr, however, the resulting heterostructures are found to exhibit a coexistence

of (240)_O and (004)_O (i.e., (001)_{pc}) orientations of PbZrO₃ from X-ray line scans (bottom two datasets, Figure 1a). This change in film orientation is accompanied by a rather substantial change of the polarization switching behavior (Figure 1d,e) where, at low electric fields (e.g., ≤750 kV cm⁻¹), antiferroelectric-like double hysteresis loops are observed, but with values of polarization smaller than those in the high-growth-pressure heterostructures. Upon increasing the electric field, however, the low-growth-pressure heterostructures gradually evolve to exhibit “ferroelectric-like” switching with considerably increased hysteresis (i.e., larger coercive fields and remnant polarization values) and the saturation polarization gradually reaches the same level (≈50 μC cm⁻²) as in high-growth-pressure heterostructures. This “ferroelectric-like” switching persists stably in the low-growth-pressure heterostructures under varied measurement frequencies (e.g., 1–10 kHz; Figure S1, Supporting Information).

To better understand what is happening, we first exclude the possibility of the emergence of a new ferroelectric phase in the low-growth-pressure heterostructures that may cause the exotic “ferroelectric-like” switching behavior. Although near-interface polar phases due to substrate strain^[28] and field-induced ferroelectric heterophases^[29] have been reported in PbZrO₃, they have only been known to cause small nonzero remanent polarization in the double-hysteresis loops and have not been shown to produce “ferroelectric-like” loops like those observed here. Further detailed reciprocal space mapping studies indicate that the low-growth-pressure heterostructures maintain the same orthorhombic structure as in the high-growth-pressure heterostructures, and no noticeable secondary phases were found in the wider-range X-ray line scans (Figure S2, Supporting Information). Moreover, the temperature-dependent dielectric constant of the low-growth-pressure heterostructures (e.g., 45 mTorr) shows a similar trend to that of the high-growth-pressure heterostructures (e.g., 80 mTorr) wherein there is only one permittivity peak at ≈280 °C corresponding to the antiferroelectric-to-paraelectric phase transition (Figure S3, Supporting Information).^[26] Second, it is also noted that the “ferroelectric-like” switching is not simply related to the (004)_O film orientation found in the low-growth-pressure heterostructures (Figure 1). Even at high growth pressures (e.g., 80 mTorr), (004)_O-oriented portions of the film emerge as the thickness of PbZrO₃ exceeds 100 nm, but such heterostructures still exhibit the typical antiferroelectric double-hysteresis loops (Figure S4, Supporting Information). We ascribe the coexistence of the (240)_O and (004)_O orientations to their similar energy values, which can be selectively stabilized by lattice mismatch, film thickness, and growth parameters. Excluding the above possibilities, we propose that the “ferroelectric-like” switching behavior in the low-pressure-growth heterostructures is actually correlated with the creation of bombardment-induced defects, which interact with the antiferroelectric-to-ferroelectric phase transition boundaries and alter the polarization switching.

To understand how changing the growth pressure can drive the evolution of defects through adatom bombardment, X-ray diffraction-based omega scans (i.e., rocking curves) about the primary (240)_O-diffraction condition of the PbZrO₃ heterostructures were conducted (Figure 2a and Experimental Section). The full-width-half-maximum (FWHM) of the rocking curves was found to increase gradually from 0.032° to 0.076° as the oxygen growth

pressure decreases from 120 to 25 mTorr, indicating a lower crystalline quality at lower growth pressures as a result of more bombardment induced defects. In a similar sense and consistent with prior observations,^[20,30] the heterostructures exhibit improved resistivity with decreasing oxygen growth pressure as measured via current-voltage studies (Experimental Section), with the low-growth-pressure heterostructures (i.e., 25 and 45 mTorr) exhibiting leakage current densities nearly three orders of magnitude lower than the high-growth-pressure heterostructures (e.g., 120 mTorr) (Figure 2b). Fitting the current–voltage leakage current data to test for different conduction mechanisms (Figure S5, Supporting Information) reveals that while in the heterostructures grown at 25 mTorr the transport is governed by interfacial Schottky emission, those grown at 45, 80, and 120 mTorr are all governed by Poole–Frenkel emission at fields >300 kV cm⁻¹ (i.e., the activation of charge carriers from defects within the heterostructure is primarily responsible for the leakage current).^[31] In turn, the activation energy can be extracted by fitting the temperature-dependent leakage current based on the Poole–Frenkel formula (Figure 2b–d)^[32] and it is found that the charge-carrier activation energy increases from ≈0.57 to ≈1.01 eV as the oxygen growth pressure decreases from 120 to 45 mTorr, indicating a shift of the dominant defect state deeper into the bandgap. We speculate that, in the heterostructures grown at 25 mTorr (with even stronger bombardment effects), the defect state can shift even deeper into the bandgap and become more difficult to activate, so that the dominant conduction mechanism switches to the Schottky emission. We also note that we attempted other measurements, such as deep-level transient spectroscopy (DLTS),^[20] to provide a more nuanced understanding of the defect types, concentrations, and energy states, but these studies were inconclusive because the overall defect concentration and defect-related conduction were not high enough (<10⁻⁶ S m⁻¹ at 200 kV cm⁻¹ even in the most conducting PbZrO₃ heterostructure grown at 120 mTorr, Figure 2b) to obtain distinguishable DLTS signals.

Nevertheless, increases of resistivity and activation energy were also observed in similarly produced PbTiO₃- and BiFeO₃-based films at low growth pressures, and the effects were attributed to a transition from individual point defects to the formation of deeper-lying defect complexes due to the production of additional intrinsic point defects via bombardment effects.^[20,30] Although it is difficult (at this time) to determine exactly what the nature of the defects are in the PbZrO₃ heterostructures, it is reasonable to assume that individual point defects are dominant for high growth pressures. The dominant defect energy state of high-growth-pressure PbZrO₃ heterostructures (e.g., ≈0.57 eV for 120 mTorr) is similar to that observed for PbTiO₃ (0.46–0.56 eV)^[20,33] and BiFeO₃ (0.60–0.80 eV),^[32,34] which are ascribed to lead vacancies and oxygen vacancies, respectively. Upon decreasing the oxygen growth pressure there should be an increase in the overall adatom kinetic energy in the growth, which means that more ions can be displaced from their ideal lattice sites in the PbZrO₃ films via bombardment effects. This, in turn, should produce a higher concentration of point defects which can interact with and compensate for each other by forming defect complexes. These defect complexes exhibit deeper trap energies than individual point defects. The dominant defect trap energy state in the low-growth-pressure PbZrO₃ heterostructures (e.g., 1.01 eV for 45 mTorr) is again close to that in ion-bombarded PbTiO₃ (0.93–1.01 eV)

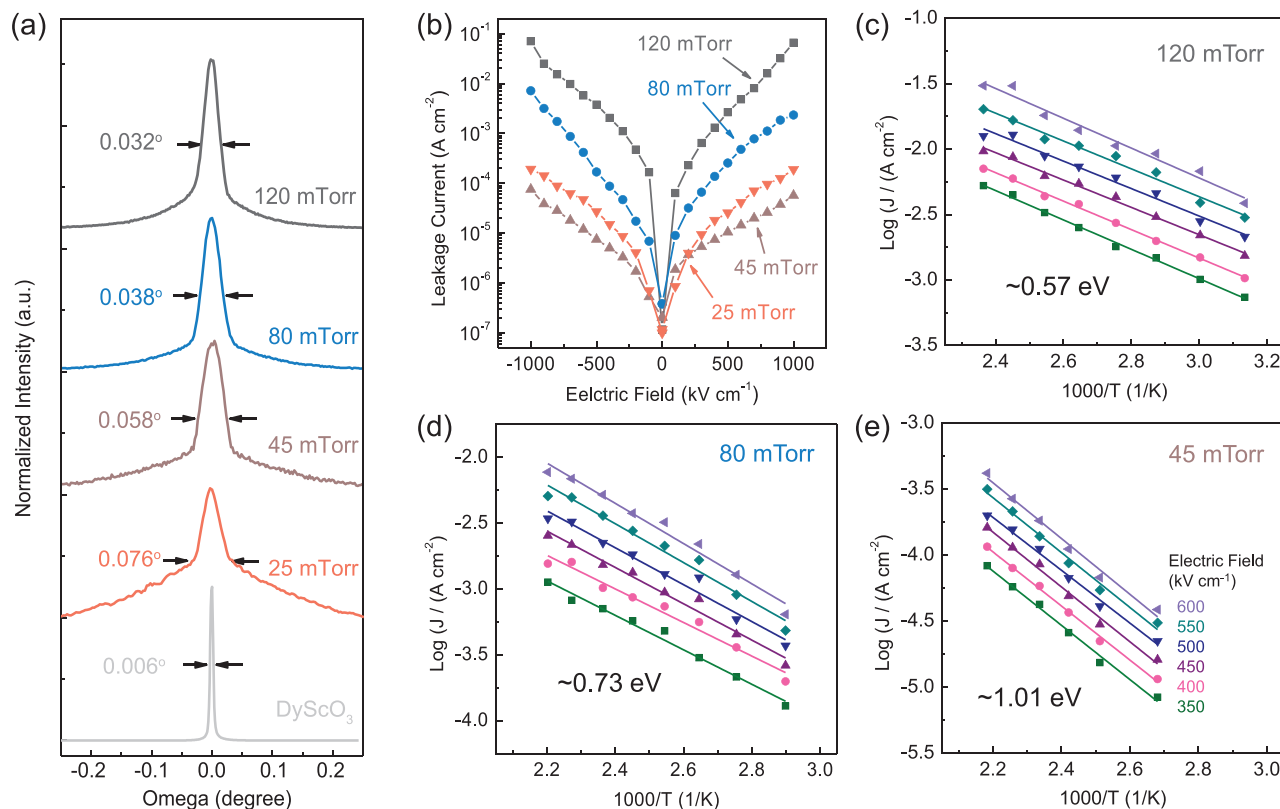


Figure 2. a) X-ray diffraction ω scans (rocking curves) about the primary $(240)_O$ -diffraction condition of the PbZrO_3 heterostructures (from top to second-from-bottom) grown at 120, 80, 45, and 25 mTorr as well as about the $(220)_O$ -diffraction condition of the DyScO_3 substrate (bottom). b) Field-dependent leakage current densities of the PbZrO_3 heterostructures grown at various oxygen pressures. c–e) Fits of temperature (T)-dependent leakage current densities (J) at varied electric fields from 350 to 600 kV cm^{-1} for the PbZrO_3 heterostructures grown at 120 mTorr (c), 80 mTorr (d), and 45 mTorr (e). The dominant charge-carrier activation energies in the heterostructures are extracted based on the Poole–Frenkel formula.

and BiFeO_3 (1.02–1.16 eV), where bombardment-induced defect complexes are believed to play a major role.^[20,32]

Acknowledging the parallels with previous studies of growth- and ion-bombardment-induced defect complexes, the “ferroelectric-like” switching in the antiferroelectric PbZrO_3 heterostructures can be better rationalized in analogy to defect-domain-wall interactions in ferroelectrics.^[35] There, point defects have been found to be more stable at domain walls^[36] and defect complexes (which possess dipole moments with collections of positively and negatively charged point defects, and are unlikely to be reoriented by external fields unless at a rather high temperature and over a rather long period)^[14,37] have been found to pin domain-wall motion.^[32,38] Analogously, in this work, such defect complexes seem to pin the antiferroelectric-to-ferroelectric phase boundaries and thus alter the polarization switching behavior. To demonstrate this, effective permittivity curves (i.e., the differential of the polarization with field based on the polarization hysteresis loops in Figure 1) for the various PbZrO_3 heterostructures were derived (Figure 3a,b; Figure S6, Supporting Information). For the high-growth-pressure heterostructures (e.g., 80 mTorr; Figure 3a), only one set of permittivity peaks is observed (i.e., $\pm E_F$ ($\approx \pm 500 \text{ kV cm}^{-1}$) and $\pm E_A$ ($\approx \pm 370 \text{ kV cm}^{-1}$)) corresponding to the antiferroelectric-to-ferroelectric and ferroelectric-to-antiferroelectric transitions, respectively, in the positive and negative branches. A schematic of the evolution of

the antiferroelectric-to-ferroelectric transitions at various applied fields for the high-growth-pressure heterostructures is provided (steps 1 to 5, Figure 3a), where there is insignificant pinning of the phase boundaries by the (predominantly) individual point defects. By comparison, in the low-growth-pressure heterostructures (e.g., 45 mTorr; Figure 3b), while similar $\pm E_F$ and $\pm E_A$ peaks are observed at low applied fields ($\leq 750 \text{ kV cm}^{-1}$), a new set of peaks ($\pm E'_F$ and $\pm E'_A$) emerges upon application of higher fields which represents delayed switching behavior (i.e., $E'_F > E_F$ and $E'_A < E_A$) and, we propose, is linked to the interaction of the bombardment-induced defect complexes with the antiferroelectric-to-ferroelectric (and vice versa) phase transition boundaries (steps I to V, Figure 3b). At an applied field between E_F and E'_F (step II, Figure 3b), regions free from pinning defect complexes transform to the ferroelectric phase, while regions with pinning defect complexes remain (at least temporarily) antiferroelectric due to the inability of the field to sweep the antiferroelectric-to-ferroelectric phase boundaries completely through the area. The pinning energy is overcome only at a higher field above E'_F where one can fully realize the phase transition to the ferroelectric state (step III, Figure 3b). Similarly, as the field is decreased to E_A , regions free from pinning defects switch back to the antiferroelectric phase as expected, while regions with pinning defect complexes remain ferroelectric (step IV, Figure 3b) until a smaller (and even a negative) field of E'_A is

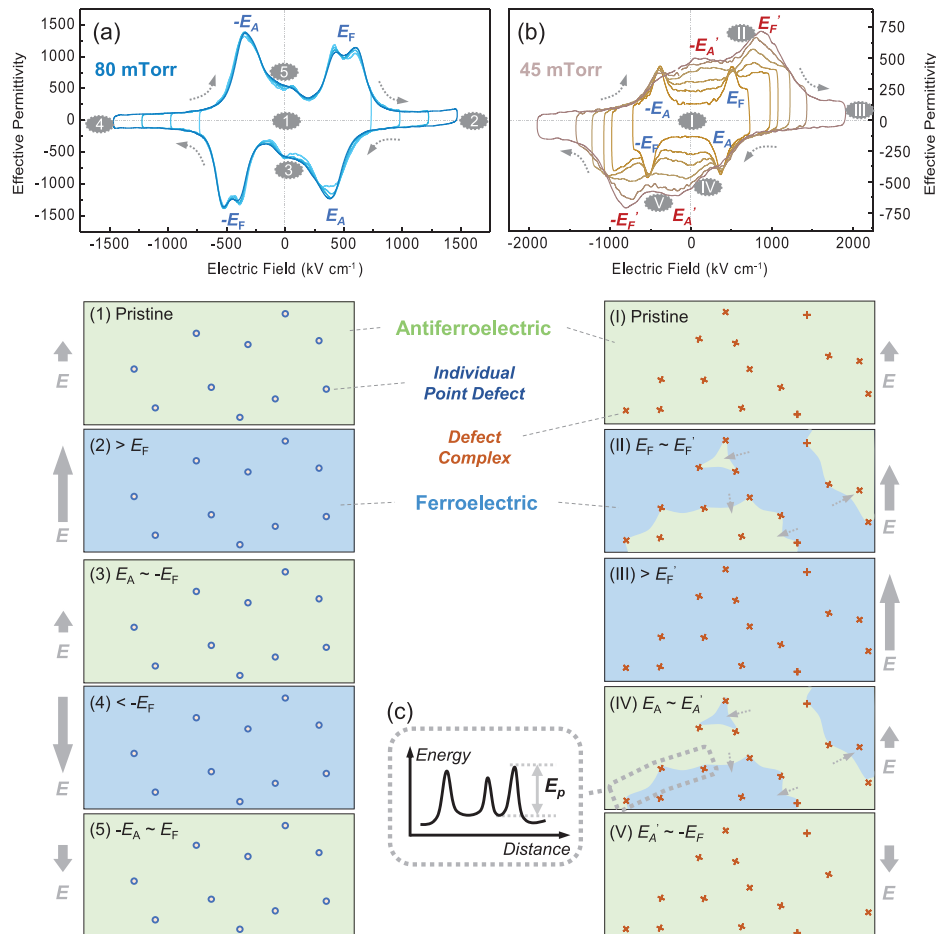


Figure 3. a) Effective permittivity curves (differential of polarization with field) of a high-growth-pressure PbZrO_3 heterostructure (80 mTorr) showing the $\pm E_F$ and $\pm E_A$ peaks, which represent the antiferroelectric-to-ferroelectric phase transitions, and are negligibly affected by the primarily individual point defects in the heterostructure, as schematically shown in steps 1–5. b) Effective permittivity curves of a low-growth-pressure PbZrO_3 heterostructure (45 mTorr) showing the additional $\pm E'_F$ and $\pm E'_A$ peaks which correspond to the onset of the delayed antiferroelectric-to-ferroelectric phase transitions due to the presence of pinning defects (complexes), as schematically shown in steps I–V. The dashed arrows indicate the directions of phase-boundary motion. c) Schematic of the local landscape for the antiferroelectric-to-ferroelectric phase boundary that results from the presence of pinning defects that produce an effective pinning energy E_p .

applied (step V, Figure 3b). The resulting “delay” of the overall phase transition by pinning-defect complexes thus causes the large remnant polarization at zero field and the unexpected “ferroelectric-like” behavior in the intrinsically antiferroelectric PbZrO_3 heterostructures (Figure 1d,e). It is also reasonable that, compared with the heterostructures grown at 45 mTorr, the heterostructures grown at 25 mTorr exhibit even more delayed phase transitions (i.e., a larger E'_F and a smaller E'_A ; Figure S6, Supporting Information) and a more “ferroelectric-like” hysteresis loop (Figure 1e) because the lower oxygen growth pressure causes stronger bombardment effects and the introduction of more defect complexes to pin the phase boundaries.

The implications of this are that the local energy landscape for the antiferroelectric-to-ferroelectric phase boundaries should look something like that shown schematically (Figure 3c), wherein the pinning defects create local energy minima that must be overcome to move the phase boundary. To quantitatively measure the effective pinning energy E_p , polarization switching kinetics studies were completed as a function of voltage pulse

magnitude and time, and temperature (Figure 4a and Experimental Section). Specifically, a first and second voltage pulse were applied to transform the antiferroelectric into the ferroelectric phase and to measure the fully switchable polarization P^* . In the following pulse-delay duration, a portion of the poled ferroelectric phase depins and switches back to the antiferroelectric state. In turn, this state is again poled by a third voltage pulse and measured as P' . The change in polarization $dP = P^* - P'$ is, thus, a measure of the pinned polarization (ferroelectric phase) by the pinning defects. In turn, $-P^*$, $-P'$, and $-dP$ can also be measured in the negative direction (Figure 4a).

For the high-growth-pressure heterostructures (e.g., 80 mTorr), dP and $-dP$ remain almost zero as the pulse field increases to as high as 1500 kV cm^{-1} (Figure 4b). This is because the individual point defects do not effectively pin the phase-transition boundary (Figure 3a) and, thus, the ferroelectric phase induced by poling fully transitions back to the antiferroelectric phase during the pulse delays when relaxation can occur and thus $P^* \approx P'$. By comparison, the dP and $-dP$ values of

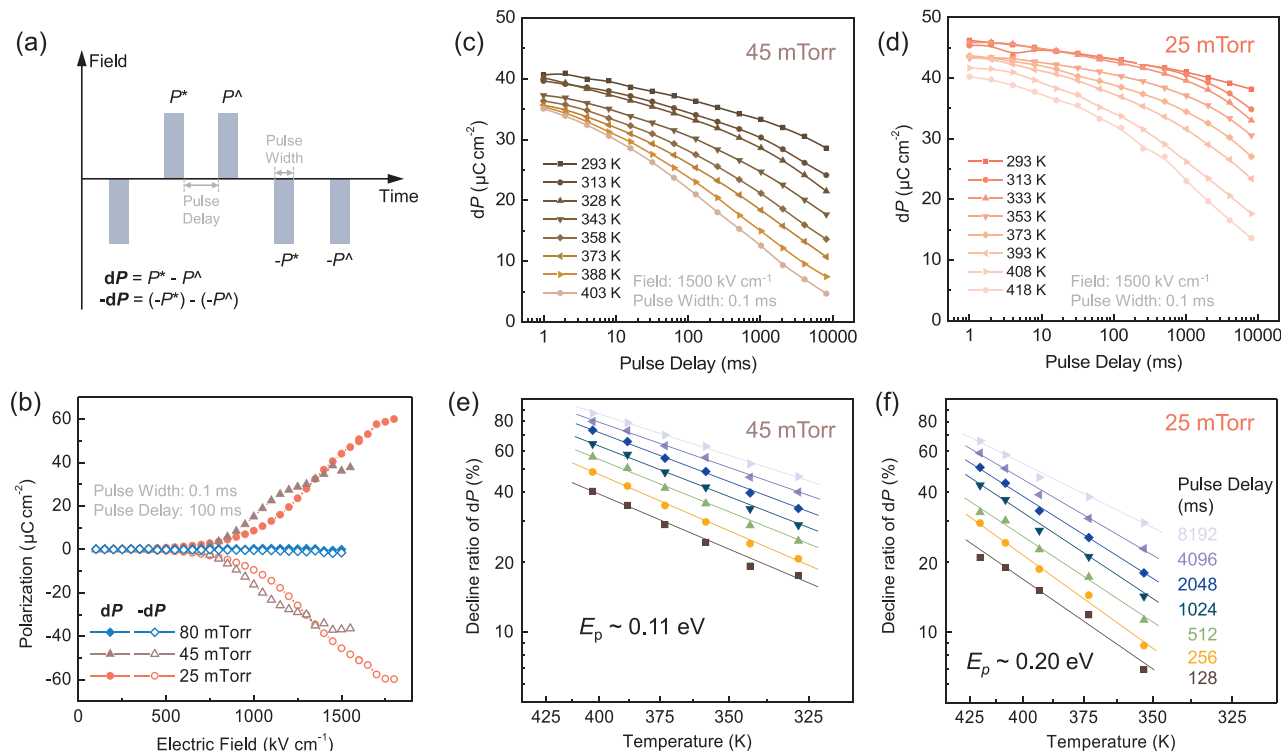


Figure 4. a) Schematic of the electric-field pulses for the switching kinetics measurement. b) The pinned polarization ($\pm dP$) in the PbZrO_3 heterostructures as a function of the pulse field for a fixed pulse width (0.1 ms) and pulse delay (100 ms). c, d) dP values as a function of pulse delay duration and temperature in PbZrO_3 heterostructures grown at 45 mTorr (c) and 25 mTorr (d). e, f) Fits of the temperature-dependent dP values for the PbZrO_3 heterostructures grown at 45 mTorr (e) and 25 mTorr (f) with an Arrhenius equation. The effective pinning energy E_p impacting the antiferroelectric-to-ferroelectric phase boundaries is thus extracted.

the low-growth-pressure heterostructures (45 and 25 mTorr) are non-zero at electric fields $>750 \text{ kV cm}^{-1}$ where pinning becomes more substantial (Figure 4b). Furthermore, with a fixed pulse field of 1500 kV cm^{-1} , the dP values of the low-growth-pressure heterostructures were found to decline over longer pulse-delay durations (Figure 4c,d), suggesting a metastability of the pinned ferroelectric phase and its tendency to depin from the pinning defects and to (ultimately) switch back to the antiferroelectric state. Unsurprisingly, this process varies with temperature, as verified by the accelerated decline of dP at elevated temperatures. The temperature-dependent dP data were found to be well fit by an Arrhenius equation (i.e., the decline of dP (in percent) was proportional to $\exp(-E_p/(k_B T))$, where k_B and T are the Boltzmann constant and temperature, respectively, and E_p is the effective pinning energy of the pinning defects (Figure 4e,f). The E_p values are extracted to be ≈ 0.11 and ≈ 0.20 eV for the PbZrO_3 heterostructures grown at 45 mTorr and 25 mTorr, respectively. The higher E_p value for the lower growth pressure is attributed to the presence of more bombardment-induced pinning defects and thus a more remarkably delayed ferroelectric-to-antiferroelectric phase transition (Figure S6, Supporting Information). It should be mentioned that, to the best of our knowledge, defect-pinning energies have not been studied in antiferroelectrics, and are also rarely reported even in the extensive experimental investigations of ferroelectrics.^[18] Theoretical calculations indicate pinning energies of ≈ 0.05 and ≈ 0.35 eV for individual point defects and defect complexes, respectively, for domain

walls in PbTiO_3 ,^[39] which are of the same order of magnitude and agree with the trends found in these PbZrO_3 heterostructures.

Finally, we demonstrate how such defects can be utilized as a novel way to engineer antiferroelectrics and to produce exotic functions. Highly tunable dielectrics are (and always have been) in great demand and are intensively sought for tunable filters, resonators, phase shifters, etc.^[40,41] Much of the research has focused on ferroelectric-based materials that exhibit “negative” tunability (dielectric constant ϵ_r that decreases with application of an external field E , i.e., $d\epsilon_r/d|E| < 0$). In contrast, antiferroelectrics like PbZrO_3 exhibit “positive” tunability (i.e., $d\epsilon_r/d|E| > 0$; Figure 5a) due to the field-induced antiferroelectric-to-ferroelectric phase transition. This “positive” tunability in PbZrO_3 persists from low frequencies (e.g., 20 kHz; Figure 5a) all the way into microwave frequencies (e.g., 1 GHz; Figure 5b); which could make these materials potentially useful for new telecommunication applications such as 5G and Internet of Things applications. Furthermore, we note that the relatively small capacitance change at microwave frequencies is the result of the in-plane interdigitated capacitor devices used for these measurements (Experimental Section and Figure S8, Supporting Information) where the parallel DyScO_3 substrate (a field-independent linear dielectric) accounts for a substantial portion of the total capacitance. Further efforts are being made for a more direct and systematic understanding of the dielectric tunability of the PbZrO_3 in the microwave frequency range.

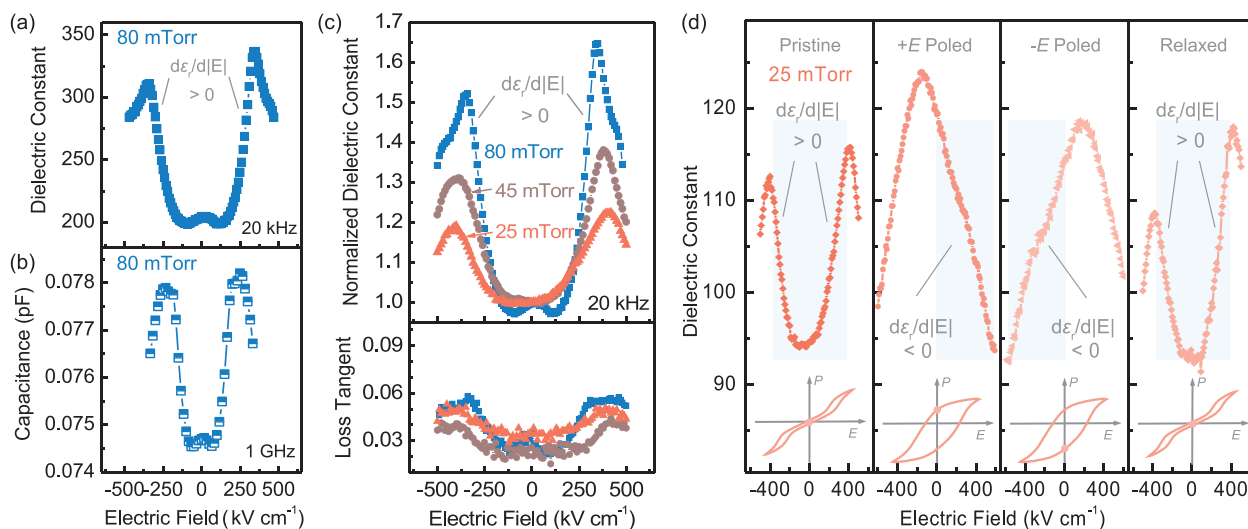


Figure 5. a,b) Electric-field-dependent dielectric constant measured at 20 kHz of a PbZrO_3 heterostructure grown at 80 mTorr (a) and capacitance measured at 1 GHz of an in-plane interdigitated capacitor device on a $\text{PbZrO}_3/\text{DyScO}_3$ (110) heterostructure (b). c) Normalized dielectric constant and dissipation (loss tangent) as a function of electric field of PbZrO_3 heterostructures grown at various oxygen pressures. The data are normalized to the films' dielectric constant at zero field for ease of comparison. d) Demonstration of the conversion of the PbZrO_3 heterostructures grown at 25 mTorr from (left to right) pristine “positive” dielectric tunability to “negative” tunability after field poling (and transformation into the “ferroelectric-like” state, either after positive or negative field poling), and then back to “positive” tunability after relaxation from the pinning defects. The light blue boxes indicate the field ranges of the “positive” or “negative” tunability. The insets schematically show the antiferroelectric and “ferroelectric-like” polarization behavior of the heterostructures in each state.

Having established the baseline properties across this wide frequency range, we further show that it is possible to adjust the dielectric tunability of the antiferroelectric by controlling the defect concentration. For example, as the deposition pressure is varied between 80 and 25 mTorr, the maximum dielectric tunability ($(\epsilon_{r,\text{max}} - \epsilon_{r,E=0})/\epsilon_{r,E=0}$) varies between $\approx 60\%$ and $\approx 20\%$, with accordingly varying slopes of the tunability and uniformly low dielectric loss (< 0.06 , Figure 5c). This performance is correlated to the controllable concentration of bombardment-induced defect complexes that pin the antiferroelectric-to-ferroelectric phase-transition boundary and alter the dielectric response. More intriguingly, in the PbZrO_3 heterostructures with a higher concentration of pinning defects, a reversible conversion between “positive” and “negative” tunability can be realized (Figure 5d). For example, while the PbZrO_3 heterostructures grown at 25 mTorr exhibit “positive” tunability in the as-grown state (pristine, Figure 5d), a pulsed voltage (e.g., $\pm 1750 \text{ kV cm}^{-1}$ for 10 ms) can transform the heterostructure into the “ferroelectric-like” phase. Consistent with the response observed before, the “ferroelectric-like” phase is (at least temporarily) sustained by the pinning defects and the material, therefore, exhibits “negative” tunability behavior ($d\epsilon_r/d|E| < 0$ at $E \geq 0$ after $+E$ poling and at $E \leq 0$ after $-E$ poling, respectively; Figure 5d). As the “ferroelectric-like” phase relaxes from defect-complex pinning and transforms back to the antiferroelectric phase after approximately minutes of time (this can be accelerated by increasing the temperature), the heterostructure again exhibits “positive” tunability (relaxed, Figure 5d). This reversible conversion of dielectric tunability is not realized in the PbZrO_3 heterostructures grown at higher pressures (i.e., with lower concentrations of defect complexes, Figure S8, Supporting Information) and is not feasible in conventional dielectrics.^[42] Thus, this concept of defect engineering provides a

new approach and a potentially promising design pathway to obtain new types of control in tunable dielectrics. Ultimately, these results highlight another example of how defects can be used as an effective knob, here in antiferroelectric materials, to develop new functionalities for potential applications.

3. Conclusions

This work reveals that point defects can strongly affect and effectively regulate the polarization switching behavior of antiferroelectrics. Unexpected “ferroelectric-like” polarization switching is observed in PbZrO_3 heterostructures deposited at relatively low oxygen pressures, which is revealed to arise from bombardment-induced defect formation that gives rise to pinning defects that work to delay (or slow down) the motion of the antiferroelectric-to-ferroelectric phase-transition boundaries. The effective pinning energy is extracted via temperature-dependent switching kinetic characterizations. Furthermore, the ability to control the sign (from positive to negative) of the dielectric tunability in the PbZrO_3 heterostructures is demonstrated by changing the concentration of the pinning defects and using voltage pulses to set the state of the material. All told, this work points to the importance of and opportunity for defects (both the type and concentration) to be used to manipulate properties in materials, in this case controlling antiferroelectric materials in new ways.

4. Experimental Section

Film Growth: 45 nm $\text{SrRuO}_3/60 \text{ nm PbZrO}_3/30 \text{ nm SrRuO}_3/\text{DyScO}_3$ (110)_O (Crystec, GmbH) thin-film heterostructures were synthesized via pulsed-laser deposition with various oxygen growth pressures (25, 45, 80,

and 120 mTorr) using a KrF excimer laser (240 nm, LPX 300, Coherent), in an on-axis growth geometry. Growth of the heterostructures was completed from ceramic targets (Praxair) of composition SrRuO₃ and PbZrO₃ with a target-to-substrate distance of ≈55 mm. The targets were sanded, cleaned, and sufficiently pre-ablated prior to each growth. The bottom electrode SrRuO₃ was deposited at a heater temperature of 700 °C in a dynamic oxygen pressure of 100 mTorr, at a laser fluence of ≈1.4 J cm⁻² and a laser repetition rate of 15 Hz. The PbZrO₃ layer was subsequently grown at a heater temperature of 600 °C in a dynamic oxygen pressure that varies in the range of 25–120 mTorr, at a laser fluence of ≈1.3 J cm⁻² and a laser repetition rate of 5 Hz. Finally, the top electrode SrRuO₃ was deposited in situ after the PbZrO₃ growth with the same growth parameters as the bottom SrRuO₃ layer, but at a reduced heater temperature of 550 °C to reduce the (potential) volatilization of lead from the PbZrO₃. The heterostructures were then cooled to room temperature at a rate of 10 °C min⁻¹ in a static oxygen pressure of 700 Torr. Following growth, capacitor structures were fabricated via photolithography and wet etching. A photoresist layer was spin-coated on the heterostructures, exposed under a photoresist mask, then developed and patterned into arrays of circles with diameters of 25 μm. The top SrRuO₃ layer was then selectively wet-etched by an NaIO₄ aqueous solution (0.1 mol L⁻¹) to realize circular capacitor structures.

Structural Characterization: X-ray line scans (2θ-ω scans and rocking curves) and reciprocal space mapping studies of the heterostructures were conducted with a high-resolution X-ray diffractometer (copper source, K_{α1} radiation of wavelength of 1.5406 Å, Panalytical, X'pert³ MRD), using a hybrid 2-bounce primary monochromator on the incident beam side and a PIXcel3D position-sensitive detector on the detector side.

(Di-)Electrical Measurements: Polarization–electric-field hysteresis loops were measured with a bipolar triangular voltage profile at a frequency of 10 kHz using a Precision Multiferroic Tester (Radiant Technologies). Leakage current densities of the heterostructures under varied DC fields up to ±1000 kV cm⁻¹ were also measured using the same Precision Multiferroic Tester, with a soak time of 200 ms followed by a measure time of 200 ms for each DC field. Dielectric permittivity data of the heterostructures as a function of frequency (5–200 kHz), DC bias field (up to ±500 kV cm⁻¹) and temperature (20–500 °C) were obtained using an impedance analyzer (E4990A, Keysight Technologies) with an oscillation AC field of 5 kV cm⁻¹. The polarization switching kinetics were measured by applying a sequence of five electric-field pulses (Figure 4a) using the Precision Multiferroic Tester, with a combination of variables: pulse amplitude, delay time, and temperature. The temperature of the samples was controlled by a customized heater (Neocera LLC) during measurement.

Microwave Device Fabrication and Measurement: A 150 nm-thick PbZrO₃ film was grown directly on a DyScO₃ (110) substrate via pulsed-laser deposition at an oxygen pressure of 80 mTorr using the conditions noted above. Following growth, in-plane, two-port interdigitated capacitor devices were fabricated on the heterostructure using a lift-off metallization process; the detailed process is provided in a previous report^[40] and a schematic structure of the device is shown (Figure S7, Supporting Information). Microwave radiofrequency dielectric measurements were performed using a four-port programmable vector network analyzer (VNA; Agilent N5227A), with an external source-measurement unit (Keithley 2634A) to apply voltage bias.

Supporting Information

Supporting Information is available from the Wiley Online Library or from the author.

Acknowledgements

The authors thank Dr. Ran Gao and Dr. Sahar Saremi for fruitful discussions. H.P., K.C., L.W., D.W., B.H., J.E.S., and L.W.M. acknowledge support from the Army/ARL via the Collaborative for Hierarchical Agile and

Responsive Materials (CHARM) under cooperative agreement W911NF-19-2-0119. Z.T. acknowledges support from the Army Research Office under grant W911NF-21-1-0118. M.A. acknowledges support from the US Department of Energy, Office of Science, Office of Basic Energy Sciences, Materials Sciences and Engineering Division under Contract No. DE-AC02-05-CH11231 (Materials Project program KC23MP) for the development of novel antiferroelectric materials. X.H. acknowledges support from the SRC-JUMP ASCENT center. H.Z. acknowledges financial support from the Department of Defense, Air Force Office of Scientific Research under Grant No. FA9550-18-1-0480. J.E.S. and L.W.M. acknowledge additional support from the Army Research Office under grant W911NF-21-1-0126.

Conflict of Interest

The authors declare no conflict of interest.

Data Availability Statement

The data that support the findings of this study are available from the corresponding author upon reasonable request.

Keywords

antiferroelectric materials, defects, dielectric tunability, polarization switching, thin films

Received: January 9, 2023

Revised: February 19, 2023

Published online: May 1, 2023

- [1] C. Kittle, *Phys. Rev.* **1951**, *82*, 5.
- [2] E. Sawaguchi, H. Maniwa, S. Hoshino, *Phys. Rev.* **1951**, *83*, 1078.
- [3] X. Hao, J. Zhai, L. B. Kong, Z. Xu, *Prog. Mater. Sci.* **2014**, *63*, 1.
- [4] A. K. Tagantsev, K. Vaideswaran, S. B. Vakhruhev, A. V. Filimonov, R. G. Burkovsky, A. Shaganov, D. Andronikova, A. I. Rudskoy, A. Q. R. Baron, H. Uchiyama, D. Chernyshov, A. Bosak, Z. Ujma, K. Roleder, A. Majchrowski, J. H. Ko, N. Setter, *Nat. Commun.* **2013**, *4*, 3229.
- [5] H. Lu, S. Glinsek, P. Buragohain, E. Defay, J. Iñiguez, A. Gruverman, *Adv. Funct. Mater.* **2020**, *30*, 2003622.
- [6] C. K. Campbell, J. D. van Wyk, R. Chen, *IEEE Trans. Compon., Packag., Manuf. Technol.* **2002**, *25*, 211.
- [7] M. Acharya, E. Banyas, M. Ramesh, Y. Jiang, A. Fernandez, A. Dasgupta, H. Ling, B. Hanrahan, K. Persson, J. B. Neaton, L. W. Martin, *Adv. Mater.* **2022**, *34*, 2105967.
- [8] D. Ko, T. Hsin, Y. Lai, S. Ho, Y. Zheng, R. Huang, H. Pan, Y. Chen, Y. Chu, *Nano Energy* **2021**, *87*, 106149.
- [9] A. S. Mischenko, Q. Zhang, J. F. Scott, R. W. Whatmore, N. D. Mathur, *Science* **2006**, *311*, 1270.
- [10] C. A. Randall, Z. Fan, I. Reaney, L. Q. Chen, S. Trolier-McKinstry, *J. Am. Ceram. Soc.* **2021**, *104*, 3775.
- [11] M. J. Pan, K. A. Markowski, S. E. Park, S. Yoshikawa, L. E. Cross, in *10th IEEE Int. Symp. on Applications of Ferroelectrics*, vol. 1, IEEE, Piscataway, NJ, USA **1996**, pp. 267–270.
- [12] H. L. Tuller, S. R. Bishop, *Annu. Rev. Mater. Res.* **2011**, *41*, 369.
- [13] H. Arandiyani, S. S. Mofarah, C. C. Sorrell, E. Doustkhah, B. Sajjadi, D. Hao, Y. Wang, H. Sun, B. J. Ni, M. Rezaei, Z. Shao, T. Maschmeyer, *Chem. Soc. Rev.* **2021**, *50*, 10116.
- [14] X. B. Ren, *Nat. Mater.* **2004**, *3*, 91.
- [15] J. H. Lee, N. X. Duong, M. H. Jung, H. J. Lee, A. Kim, Y. Yeo, J. Kim, G. H. Kim, B. G. Cho, J. Kim, F. U. H. Naqvi, J. S. Bae, J. Kim, C. W.

- Ahn, Y. M. Kim, T. K. Song, J. H. Ko, T. Y. Koo, C. Sohn, K. Park, C. H. Yang, S. M. Yang, J. H. Lee, H. Y. Jeong, T. H. Kim, Y. S. Oh, *Adv. Mater.* **2022**, *34*, 2205825.
- [16] A. Dasgupta, S. Saremi, X. Ruijuan, L. R. Dedon, S. Pandya, A. R. Damodaran, L. W. Martin, *J. Mater. Chem.* **2018**, *6*, 10751.
- [17] A. R. Damodaran, E. Breckenfeld, Z. Chen, S. Lee, L. W. Martin, *Adv. Mater.* **2014**, *26*, 6341.
- [18] S. Saremi, R. Xu, F. I. Allen, J. Maher, J. C. Agar, R. Gao, P. Hosemann, L. W. Martin, *Phys. Rev. Mater.* **2018**, *2*, 84414.
- [19] A. Fernandez, M. Acharya, H. Lee, J. Schimpf, Y. Jiang, L. Djamila, Z. Tian, L. W. Martin, *Adv. Mater.* **2022**, *34*, 2108841.
- [20] S. Saremi, R. Xu, L. R. Dedon, J. A. Mundy, S. Hsu, Z. Chen, A. R. Damodaran, S. P. Chapman, J. T. Evans, L. W. Martin, *Adv. Mater.* **2016**, *28*, 10750.
- [21] S. Saremi, R. Gao, A. Dasgupta, L. W. Martin, *Am. Ceram. Soc. Bull.* **2018**, *97*, 16.
- [22] D. Lee, H. Lu, Y. Gu, S. Y. Choi, *Science* **2015**, *349*, 1314.
- [23] M. Hofling, X. Zhou, L. M. Riemer, E. Bruder, B. Liu, L. Zhou, P. B. Groszewicz, F. Zhuo, B. X. Xu, K. Durst, X. Tan, D. Damjanovic, J. Koruza, J. Rodel, *Science* **2021**, *372*, 961.
- [24] J. Kim, S. Saremi, M. Acharya, G. Velarde, E. Parsonnet, P. Donahue, A. Qualls, D. Garcia, L. W. Martin, *Science* **2020**, *369*, 81.
- [25] E. Sawaguchi, *J. Phys. Soc. Jpn.* **1952**, *7*, 110.
- [26] C. Milesi-Brault, N. Godard, S. Girod, Y. Fleming, B. El Adib, N. Valle, S. Glinšek, E. Defay, M. Guennou, *Appl. Phys. Lett.* **2021**, *118*, 042901.
- [27] R. Gao, S. E. Reyes-Lillo, R. Xu, A. Dasgupta, Y. Dong, L. R. Dedon, J. Kim, S. Saremi, Z. Chen, C. R. Serrao, H. Zhou, J. B. Neaton, L. W. Martin, *Chem. Mater.* **2017**, *29*, 6544.
- [28] A. R. Chaudhuri, M. Arredondo, A. Haehnel, A. Morelli, M. Becker, M. Alexe, I. Vrejoiu, *Phys. Rev. B* **2011**, *84*, 54112.
- [29] R. G. Burkovsky, G. A. Lityagin, A. E. Ganzha, A. F. Vakulenko, R. Gao, A. Dasgupta, B. Xu, A. V. Filimonov, L. W. Martin, *Phys. Rev. B* **2022**, *105*, 125409.
- [30] H. Pan, N. Feng, X. Xu, W. Li, Q. Zhang, S. Lan, Y. Liu, H. Sha, K. Bi, B. Xu, J. Ma, L. Gu, R. Yu, Y. Shen, X. R. Wang, J. L. MacManus-Driscoll, C. Chen, C. Nan, Y. Lin, *Energy Storage Mater.* **2021**, *42*, 836.
- [31] J. G. Simmons, *J. Phys. D: Appl. Phys.* **1971**, *4*, 613.
- [32] S. Saremi, R. Xu, L. R. Dedon, R. Gao, A. Ghosh, A. Dasgupta, L. W. Martin, *Adv. Mater. Interfaces* **2018**, *5*, 1700991.
- [33] Z. Zhang, P. Wu, L. Lu, C. Shu, *Appl. Phys. Lett.* **2006**, *88*, 142902.
- [34] S. J. Clark, J. Robertson, *Appl. Phys. Lett.* **2009**, *94*, 022902.
- [35] D. Lee, B. C. Jeon, S. H. Baek, S. M. Yang, Y. J. Shin, T. H. Kim, Y. S. Kim, J. Yoon, C. B. Eom, T. W. Noh, *Adv. Mater.* **2012**, *24*, 6490.
- [36] T. Rojac, A. Bencan, G. Drazic, N. Sakamoto, H. Ursic, B. Jancar, G. Tavcar, M. Makarovic, J. Walker, B. Malic, D. Damjanovic, *Nat. Mater.* **2017**, *16*, 322.
- [37] H. Geng, K. Zeng, B. Wang, J. Wang, Z. Fu, F. Xu, S. Zhang, H. Luo, D. Viehland, Y. Guo, *Science* **2022**, *378*, 1125.
- [38] Q. Tan, J. Li, D. Viehland, *Appl. Phys. Lett.* **1999**, *75*, 418.
- [39] A. Chandrasekaran, D. Damjanovic, N. Setter, N. Marzari, *Phys. Rev. B* **2013**, *88*, 214116.
- [40] C. Lee, N. D. Orloff, T. Birol, Y. Zhu, V. Goian, E. Roca, R. Haislmaier, E. Vlahos, J. A. Mundy, L. F. Kourkoutis, Y. Nie, M. D. Biegalski, J. Zhang, M. Bernhagen, N. A. Benedek, Y. Kim, J. D. Brock, R. Uecker, X. X. Xi, V. Gopalan, D. Nuzhnyy, S. Kamba, D. A. Muller, I. Takeuchi, J. C. Booth, C. J. Fennie, D. G. Schlom, *Nature* **2013**, *502*, 532.
- [41] Z. Gu, S. Pandya, A. Samanta, S. Liu, G. Xiao, C. J. G. Meyers, A. R. Damodaran, H. Barak, A. Dasgupta, S. Saremi, A. Polemi, L. Wu, A. A. Podpirka, A. Will-Cole, C. J. Hawley, P. K. Davies, R. A. York, I. Grinberg, L. W. Martin, J. E. Spanier, *Nature* **2018**, *560*, 622.
- [42] A. Ahmed, I. A. Goldthorpe, A. K. Khandani, *Appl. Phys. Rev.* **2015**, *2*, 011302.